Gas-phase synthesis of plasmonic nanoparticles with robust high band-gap shell materials: a study of Cu@CaF_2 with Al supported transmission electron microscopy analysis

Eleonora Spurio[1,2], Enzo Rotunno[2], Paolo Rosi[2], Samuele Pelatti[1,2], Guido Paolicelli[2], Andrea Mescola[2], Gian Carlo Gazzadi[2], Paola Luches[2] and Sergio D'Addato[1,2,3*]

[1]Dipartimento Scienze Fisiche, Informatiche e Matematiche, Università di Modena e Reggio Emilia, via G. Campi 213/a, 41125 Modena, Italy

[2]CNR, Istituto Nanoscienze, via G. Campi 213/a, 41125 Modena, Italy

[3]En&Tech, via G. Campi 213/a, 41125 Modena, Italy

[*]Corresponding author, sergio.daddato@unimore.it

Keywords: plasmonic nanoparticles, copper, calcium difluoride, Al supported TEM analysis

Highlights

1. First gas-phase synthesis of Cu@CaF_2 plasmonic nanoparticle films.
2. Automated Mask R-CNN analysis provided precise nanoparticle size and shape statistics.
3. The morphology of Cu nanoparticles is unmodified by thin CaF_2 coverages.
4. CaF_2 shells improve nanoparticle stability and preserve plasmonic properties.
5. Stable optical properties after long-term exposure to atmosphere.

Cu@CaF_2 plasmonic nanoparticle (NP) films are physically synthesized, and their morphology, electronic, and optical properties are thoroughly investigated. Cu NPs are generated using a gas aggregation source assisted by magnetron sputtering, while CaF_2 coatings are deposited by thermal evaporation. Scanning Electron Microscopy (SEM), Atomic Force Microscopy (AFM), and Transmission Electron Microscopy (TEM) provide a clear picture of the film morphology. The Cu NP shapes remain substantially unaffected by the deposition of CaF_2, acting as nucleation centers for fluoride growth, which effectively forms a protective shell. With increasing CaF_2 thickness, the shells extend to form islands, which eventually coalesce into a complex film morphology. Computer vision methods based on Mask R-CNN, one of the leading deep learning architectures for object detection, are employed to fully automate particle analysis, exploiting its capabilities to perform detailed statistical evaluation of NP size and shape from a large number of images. AFM and TEM reveal that the NPs have a lateral size of $\langle d \rangle = 13.8 \pm 0.9$ nm and an oblate spheroid shape with an aspect ratio $AR = d/h \approx 1.2$. In situ XPS data show that the chemical state of the NPs is unaffected by the presence of CaF_2. Finally, optical data obtained with a UV-Vis-Near IR spectrometer and simulated using the Maxwell-Garnett approximated extinction cross section demonstrate that the Cu localized surface plasmon resonance remains robust under prolonged atmospheric exposure, a fundamental property that is crucial for applications in photovoltaics and optoelectronics.

1. Introduction

Noble metal nanoparticles (NPs) have attracted increasing interest in recent years in a wide range of different fields, including photovoltaics [1, 2, 3], biosensing [4], catalysis and photocatalysis [5, 6, 7], magnetic recording [8] and optoelectronics [9, 10], thanks to novel and relevant properties distinct from their bulk forms [11]. In particular, plasmonic NPs have unique optical properties, related to the excitation of localized surface plasmon resonances (LSPRs) [1]. This phenomenon involves a collective resonant excitation of charges, resulting in intense spectral absorption and scattering, along with significant electromagnetic near-field enhancements at the resonance frequency. Notably, the LSPR frequency of noble metal NPs like Ag, Cu and Au can be tuned in the ultraviolet-visible-near infrared (UV-vis-NIR) region [6, 11]. Compared to other noble metals, copper is an abundant and low-cost material [12]. The main limitation of Cu in terms of plasmonic applications is related to its strong reactivity to oxygen, which makes it unstable in atmospheric conditions. To enhance the stability of Cu by reducing its sensitivity to oxygen, water, and other chemicals, Cu-based NPs with more complex architectures have been developed and investigated [10, 12]. These include for example core@shell Cu NPs and nanostructured systems based on copper oxides [13, 14, 15, 16]. Besides stabilizing the plasmonic properties, the combination of NPs and dielectric materials also permits to tune the LSPR frequency by varying the dielectric material and thickness [16, 17]. Moreover, the choice of a high band-gap material is due to the necessity of preserving the chemical stability of Cu and to the possibility of the material to be transparent in the visible and UV radiation for their employment in photovoltaic materials. The plasmonic properties of the NPs not only depend on their dielectric environment but are also influenced by their morphology; the LSPR frequency can be tuned by varying the size, the shape and the aspect ratio (AR) of the NPs [18, 19]. The deposition of preformed NPs generated by gas phase synthesis permits to finely tune the characteristics of the NPs by fine adjustment of the parameters governing the growth conditions providing NPs with variable size distribution, density and structure. In previous works by some of the authors [15, 16, 17, 18, 19], different combinations of plasmonic materials and dielectric coatings have been investigated. In the present work, Cu NPs have been grown by a gas aggregation cluster source based on magnetron sputtering. The NPs were then coated with films of CaF_2 with different thicknesses. CaF_2 is a very appealing material for optical components. In fact, its wide bandgap (above 12 eV [20]) makes it transparent in a wide range of wavelengths, from ultraviolet (UV) to infrared (IR). Furthermore, compared to other materials, widely studied as protective coatings for plasmonic NPs, such as Al_2O_3, MgO or SiO_2, CaF_2 is characterized by a uniquely low refractive index, that strongly reduces reflection losses [21]. This makes CaF_2 the most commercially important material within the optics community [22]. Moreover, CaF_2 is chemically inert and resistant to corrosion, non-toxic and mechanically robust.

This study aims to explore the influence of the CaF_2 top-layer thickness on the morphological, electronic, and optical properties of Cu@CaF_2 NPs, with particular emphasis on understanding the

stability and potential enhancements in optical performance introduced by the CaF_2 capping layer. It also opens possibilities to design new architectures of plasmonic nanostructures to be applied in photovoltaics and optoelectronics.

2. Experimental

Films composed by Cu NPs combined with thin films of CaF_2 of different thicknesses were prepared, to characterize the effects of the protective coating on the plasmonic properties of the NPs, in terms of resonance frequency and stability. In situ X-ray Photoelectron Spectroscopy (XPS) was used to study the electronic properties and the chemical state of the investigated samples. The morphology of the films was studied by means of Scanning Electron Microscopy (SEM), Atomic Force Microscopy (AFM) and Transmission Electron Microscopy (TEM). Finally, the optical properties of the systems were examined by means of Ultraviolet-Visible (UV-Vis) absorbance spectroscopy. The morphological characterization of the Cu NPs with TEM and AFM has been performed by using the same nanocluster source conditions used to grow the sample for the optical characterization, except for the lower amount of deposited Cu NPs. The lower density allows to better distinguish individual NP and permits a more detailed characterization.

Cu NPs and Cu@CaF_2 NPs films were prepared in the experimental apparatus described in [23]. Cu NPs were physically synthesized by using a magnetron sputtering nanocluster source with inert gas aggregation (NC200U, Oxford Applied Research) in an Ar gas flow value f= 60 sccm, and source power P=42 W. The NP beam was focused and size selected by using a quadrupole mass filter (QMF200, Oxford Applied Research) before reaching the chosen substrate. The source working conditions were the same as the ones described in ref. [14]. In that work, an analysis of the size distribution of bare Cu NPs deposited on Si/SiO_x provided an average lateral size $<d>=11.4$ nm, and the size dispersion of the distribution was found to be $\Delta d= 3.3$ nm. A thermal evaporation source was used to deposit the CaF_2 film on top of the NPs (thermal source power=147 W). The thickness of the Cu NPs and CaF_2 films was controlled by means of a quartz crystal microbalance, which was used to estimate the deposition rates from the nanocluster source and from the evaporator before the growth. The CaF_2 deposition rate ranged between 4 and 6 Å/min and the Cu NPs deposition rate varied between 0.5 and 2 Å/min. Here, the deposition rate and the amount of deposited Cu NP are given in terms of equivalent values for a continuous film. The samples investigated in the present work differ in Cu NP density and/or CaF_2 shell thickness because the different characterization techniques employed, require specific sample architectures to achieve optimal signal and resolution. For microscopy characterization, samples with low density of NPs (1-2 nm) are required to resolve the individual nanoparticles, whereas spectroscopic measurements benefit from higher NP densities to improve the signal-to-noise ratio. Different CaF_2 film thicknesses were used to investigate the shell growth morphology.

The deposition chamber is connected to a second vacuum chamber equipped with an X-ray source (XR50, Specs), generating Mg Kα photons, and an electron hemispherical analyzer (Phoibos 150, Specs) for in-situ chemical characterization. The SEM images were acquired by a FEI Nova Nano SEM450. The SEM column is equipped with a Schottky field-emission gun (SFEG), and it can achieve a resolution of 1.4 nm in a low-voltage (1 kV) operation. The TEM images were obtained by high resolution transmission electron microscopy (HRTEM) imaging with a ThermoFisher Talos FS200 equipped with a SFEG at 200 kV. Finally, AFM images were taken with an NT-MDT microscope model NTEGRA AURA, in semi-contact (tapping) mode with Si cantilevers. The setup for the optical characterization included a Xenon lamp providing white non-polarized light, an ORIEL-MS257 monochromator, a polarizer, and a silicon photodetector. The absorptance (A) of the sample is determined by the formula A = 1-(T+R), where T and R represent the transmittance and reflectance, respectively. These measurements were taken with the incident photon beam at an angle of 22° to the sample surface normal. In this setup, s polarization lies entirely in the surface plane, while p polarization includes a small out-of-plane component. To compare the experimental results with theoretical expectations, the extinction cross section has been calculated by performing polarizability simulations using the MNPBEM MATLAB toolbox [24]. The NPs have been assumed to be oblate spheroids with AR derived from combining the information obtained for the in-plane dimensions from the SEM/TEM images and the out-of-plane dimensions from the AFM analysis. For the simulations, the bulk dielectric functions were obtained from [25] for Cu, from [26] for CaF_2, while the real part of the complex refractive index for quartz was calculated using the Sellmeier equation [27] applied to fused SiO_2 at room temperature [28].

The substrates used during the experiments were Si/SiO_x wafers for SEM and AFM measurements, Uv-grade fused silica substrate for the optical experiments, and C-coated Ni grids for TEM observations. However, the manual measurements of a large number of particles is still a painstaking process prone to human error.

Other conventional particle analysis methods, such as threshold-based segmentation, or watershed algorithms, often require extensive manual tuning and are sensitive to imaging conditions like contrast variations and noise. These methods also struggle to accurately segment overlapping particles and may introduce user bias through manual intervention.

To overcome this challenge, a Mask Regional Convolutional Neural Network (Mask R-CNN) [29] has been employed. Mask R-CNN has demonstrated superior accuracy in measuring particle size distribution [30-32] and in the instance segmentation of electron microscopy image data [33-36]. These advantages make it particularly suitable for large-scale or time-resolved studies where consistency and efficiency are critical.

Object detection using Mask R-CNN is a supervised machine learning method, which requires extensive annotated training data before it can accurately detect NPs. In this study we used the official implementation of Mask R-CNN from the TensorFlow Model Garden [37]. It is based on a

MobileNetV2 backbone pretrained on the COCO dataset, followed by a region proposal network (RPN) and two instance segmentation heads. The RPN generates candidate regions of interest (RoIs) likely to contain particles from the feature maps obtained by combining different layers of the backbone. These RoIs are refined by a two-stage head: one for object classification and bounding box regression, and another for predicting a binary mask for each detected instance. The model was trained using a cosine learning rate schedule with linear warmup, and optimization was performed using stochastic gradient descent with a batch size of 8 for 200 epochs. The network was trained on a single TEM image (resolution 4096×4096) containing 243 particles manually annotated to delineate the Cu cores using freely available software [38]. To enhance the training dataset, it was artificially augmented by rotating and shifting the nanoparticles, bringing the total count of element up to 2145. The model was fine-tuned over 2000 epochs using a cosine learning rate decay with linear warmup:200 steps warmup, starting at a learning rate of 0.05, increasing to an initial peak of 0.07, then decayed following the cosine schedule until the end of training.

Although the small training dataset size might limit the model's generalizability, the homogeneity of the studied sample mitigates this concern for the specific context of this study. Low-magnification imaging minimized variability in illumination and focus, and particle orientation had minimal impact due to the lack of high-resolution features. The continuous thin carbon film ensured clear particle contrast, while the CaF_2 shell was effectively invisible at the analyzed magnifications. Edge artifacts and rare overlapping particles were excluded or manually corrected. The only remaining bias arises from manual annotation, limited to a few pixels and not affecting conclusions.

The Mask R-CNN performance was evaluated on a validation set using standard COCO metrics [39], which are commonly used to quantify object detection and instance segmentation performance. These metrics are based on the intersection-over-union (IoU) between predicted and manually annotated masks. The AP@[0.50:0.95] value represents the average precision computed over multiple IoU thresholds, from 0.50 to 0.95, and therefore provides a stringent measure of both particle detection and mask accuracy. AP@0.50 is a more permissive detection metric, while AP@0.75 gives a stricter indication of localization and segmentation quality. Average recall (AR) measures the fraction of ground-truth objects that are successfully detected, while the F1 score summarizes the balance between precision and recall.

The obtained validation metrics were very high: AP@[0.50:0.95] = 0.89, AP@0.50 = 0.97, AP@0.75 = 0.93, AR@[0.50:0.95] = 0.90, and F1@[0.50:0.95] = 0.89. The AP@0.50 value close to unity indicates that almost all particles are correctly detected at moderate IoU tolerance, while the high AP@0.75 shows that the predicted masks also reproduce the particle contours with good accuracy. The high AR value indicates that only a small fraction of particles is missed, and the F1 score confirms that the model achieves a good balance between false positives and false negatives.

These values are substantially higher than those typically obtained on the general COCO benchmark, but this comparison must be interpreted correctly. The present task is much more

constrained than generic object detection: it involves a single object class, homogeneous Cu nanoparticles, stable low-magnification TEM imaging conditions, and strong particle/background contrast. Therefore, the high metrics should not be interpreted as evidence of universal generalizability to arbitrary nanoparticle systems or imaging conditions. Rather, they demonstrate that, for the specific and well-defined segmentation task required in this work, the trained Mask R-CNN model performs exceptionally well and provides a reliable basis for automated statistical analysis of Cu nanoparticle size distributions.

All training data, annotation files, configuration files, and Jupyter notebooks with full training parameters are publicly available (see Data Availability section), making the workflow fully repeatable.

3 Results and Discussion

3.1 Morphology

Figure 1 shows the SEM image of a CaF_2 film of 18 nm grown on a Si substrate, without Cu NPs. This preliminary analysis was necessary to understand the morphology of the CaF_2 film grown via thermal evaporation.

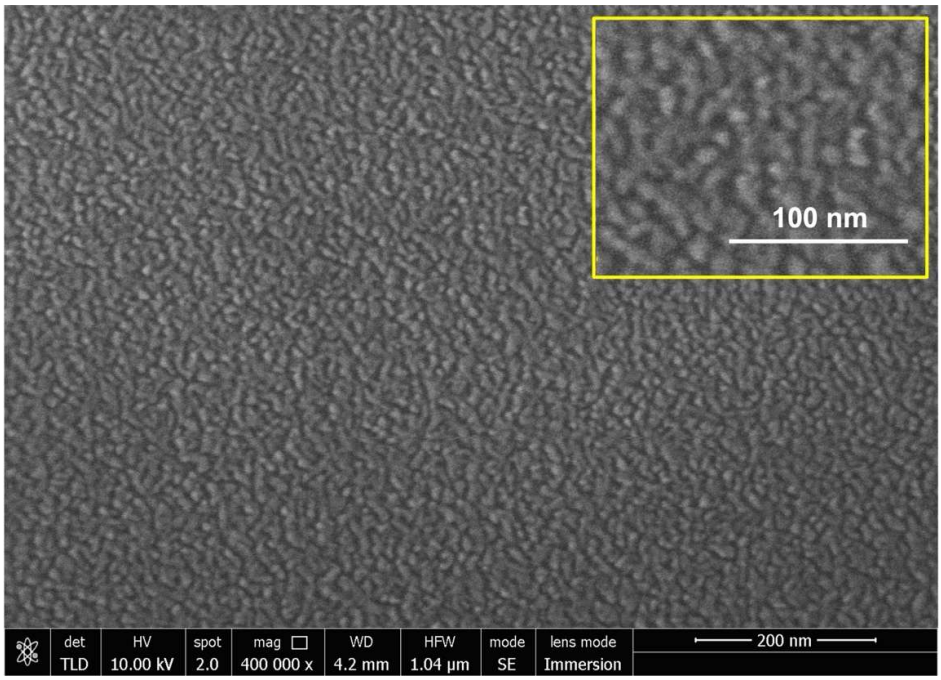

Figure 1. SEM image of a CaF_2 film (18 nm) deposited on Si/SiO_x.

Figure 1 shows that CaF_2 forms an islanded layer with islands of approximately 5-20 nm size, as observed in a previous work [17]. To better evidence the islanded structure, the inset in Figure 1 shows a portion of the sample imaged using a higher magnification. The morphology of Cu NPs combined with the CaF_2 film was then investigated. Different films have been considered: a sample composed by CaF_2/Cu NPs/CaF_2 layers and two samples composed by Cu NPs and capped by

CaF_2 films with two different thicknesses. The corresponding SEM images are shown in Figure 2: Figure 2 (a) represents the SEM image of the CaF_2/Cu NP/CaF_2 with $t^{(1)}_{CaF2}$=1.5 nm, t_{Cu}= 1 nm and $t^{(2)}_{CaF2}$=1.5 nm. The distribution of the NPs diameter is shown in Figure 2 (b), together with the lognormal distribution used to fit the histogram: the size distribution has a maximum at 16.2 nm, while the average diameter is 17.7 nm with a standard deviation of 3.4 nm. Figure 2 (c) reports the image of a sample composed by a Cu NPs film with t_{Cu}=2 nm covered by a CaF_2 thin film t_{CaF2}=0.5 nm. Figure 2 (d) shows the diameter distribution of NPs in this sample, together with the lognormal distribution used to fit the histogram: the size distribution has a maximum around 14 nm, while the average diameter is 16.4 nm with a standard deviation of 3.2 nm.

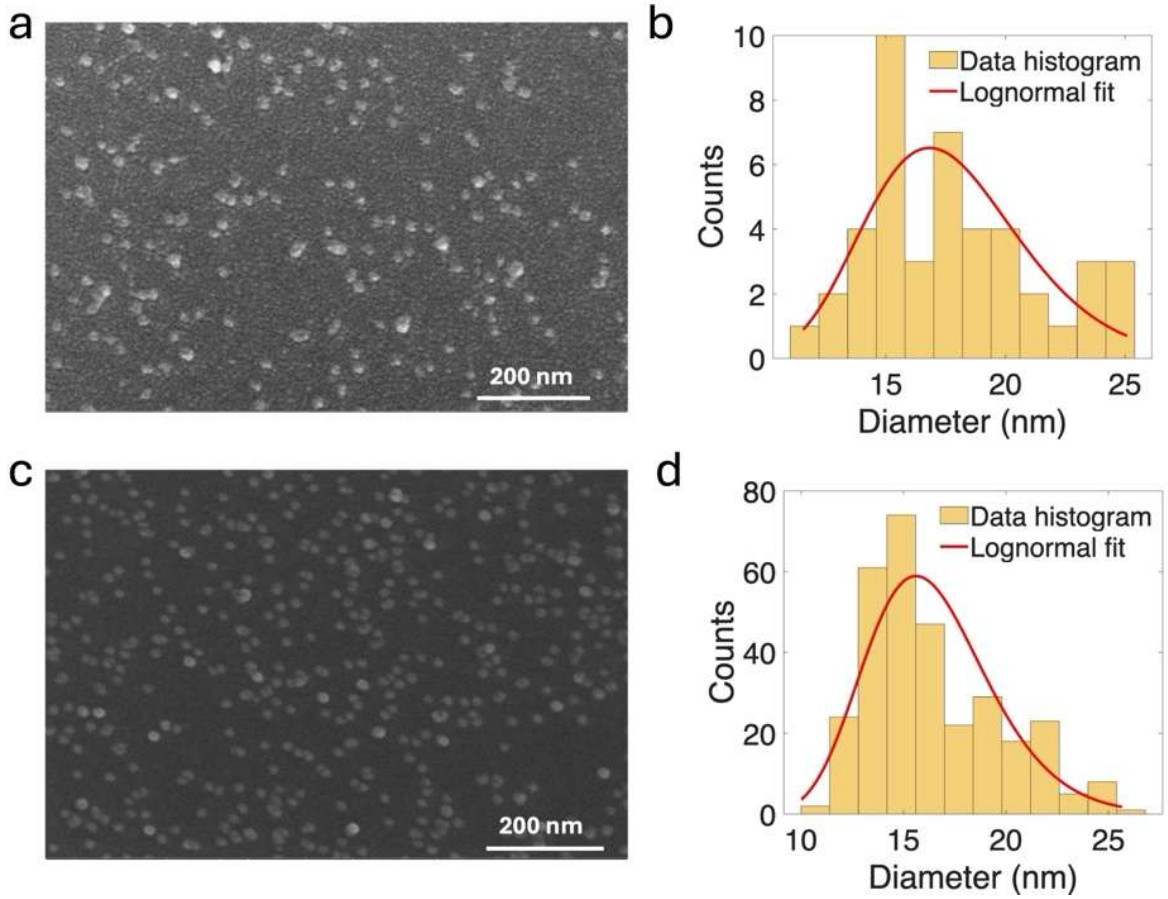

Figure 2 (a) SEM image and (b) diameter distribution of Cu NPs of CaF_2/Cu NP/CaF_2 sample (1.5 nm/1 nm/1.5 nm) and (c) SEM image and (d) diameter distribution of Cu NPs of the Cu NP/CaF_2 sample (2 nm/0.5 nm) deposited on Si/SiO_x substrates.

The main difference between Figure 2 (a) and 2 (b) is the fractional coverage F (related to the NP surface density), which is F ≃ 11% in the first sample and F ≃ 17% in the second one. This difference in coverage is a consequence of in the amount of the Cu NPs deposited in the two samples. Also, an increased roughness of the substrate in Figure 2 (a) can be observed, caused by the first layer of CaF2, which was grown before the deposition of Cu NP. In Figure 2 (c) the thin CaF_2 layer is not

distinguishable, and it possibly nucleates close to the NPs. Although the amount of Cu NPs in the two figures is different, the morphology of the NPS in the two samples are extremely similar, as demonstrated by the diameter distributions shown in Figure 2 (b) and Figure 2 (d), coherently with the fact that the Cu NPs are pre-formed before reaching the substrate, so that the morphology of the Cu NPs is independent on the substrate composition, material and roughness. The lognormal fit of the two size distributions reported in fig.s 2c) and 2d) gives a slight difference between the two average diameters, caused probably by the thinner CaF_2 shell in the sample of figure 2c. The situation changes dramatically when the NPs are covered by a thicker CaF_2 layer. SEM images of a sample composed by a layer of Cu NPs of nominal thickness t_{Cu}=1 nm covered by a CaF_2 film with thickness t_{CaF2}=7 nm are shown in Figure 3. We can recognize a more complex morphology at higher CaF_2 coverage with respect to the case of thinner capping layers. The islands have extended over the whole sample, instead of forming a covering shell around the NPs as in the case of lower coverage, and the Cu NPs are completely buried under the CaF_2 layer.

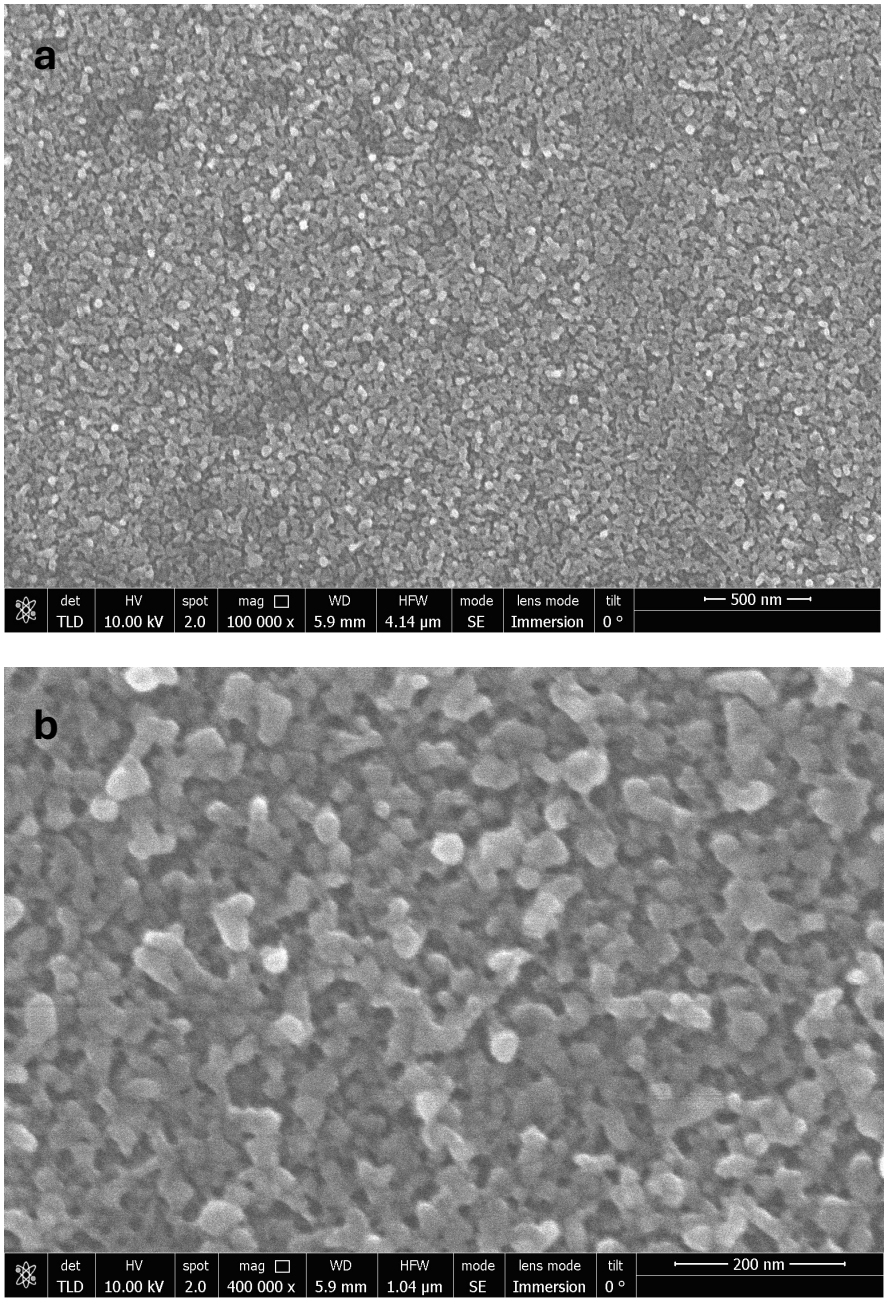

Figure 3. a) SEM image of a Cu NP/CaF_2 sample (1 nm/7 nm) taken with magnification 100 000X. b) Image taken from the sample taken with magnification 400 000 X.

It is interesting to note that the island shapes are completely different from the ones observed in Figure 1, where the CaF_2 film is much more uniform. This is due to the presence of Cu NPs, acting as nucleation centers for the CaF_2 overlayer. CaF_2 is preferentially absorbed at the nanocluster surfaces, becoming an effective shell material. When the amount of deposited CaF_2 increases, the islands extend and coalesce, with a non-uniform growth mode. The actual position of the Cu NPs is difficult to be observed after the CaF_2 deposition, as the extension of the CaF_2 islands covers probably more than one particle.

Figure 4a shows a 1 μm x 1 μm AFM image of the sample composed of t_{Cu} =2 nm of Cu NPs covered by a film with t_{CaF2}=0.5 nm deposited on Si/SiO_x. The results of the grain analysis applied to the image in Figure 4a are shown in Figure 4b. The height statistical distribution was fitted with a Gaussian, giving an average height <h>=11±2 nm. The NPs height distribution values are relative to the Si/SiO_x substrate which is characterized by a roughness S_q = 1.2 nm. The height distribution measurements were referred to the Si/SiO_x substrate because the CaF_2 films on the substrate is not uniform, as it can be seen if figure 1. This morphology could affect the results obtained by AFM. The different average values obtained for the lateral NP size distribution as obtained by SEM and for the height as obtained by AFM can be ascribed to various reasons:

1. The CaF_2 coverage can affect the morphology of the “naked” Cu NPs, increasing the overall lateral size of the nanoparticles.
2. The worse lateral resolution of the SEM measurement (ΔD=2 nm), compared with the height resolution of AFM (estimated to be Δh=0.5 nm) can be responsible for the higher aspect ratio observed.
3. The Cu NP films grow in a random paving mode, as observed in previous works, giving rise to coalescence of two or more NPs when they are deposited on the same or on close sites. The coalescence of Cu NPs can also occur during the formation of the NP beam in the source.
4. There also could be an electrostatic interaction between the NPs and the substrate, the NP being mostly negatively charged, (as measured by the QMF) and the Si/SiO_x substrate having an insulating oxide top layer [40,41].

We note that this AR value is an indirect, ensemble-averaged estimate obtained by combining complementary TEM and AFM measurements, and it is used here as an effective geometrical parameter for the optical simulations rather than as a direct 3D reconstruction of individual nanoparticles.

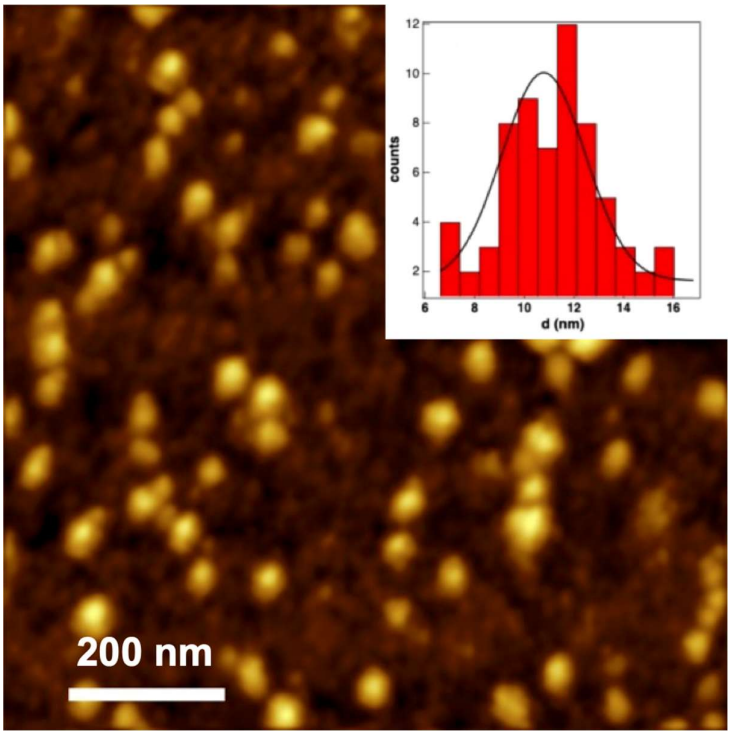

Figure 4. AFM topography image of a Cu NPs / CaF_2 sample (2 nm/0.5 nm) deposited on Si/SiOx. Inset: NPs height distribution (histogram) relative to the Si/SiOx substrate and gaussian fitting curve (black).

A TEM analysis has provided information on the NP average lateral size with higher resolution than SEM. This piece of information combined with the NP height measured by AFM, allows to estimate the aspect ratio of the NPs. A sample with a low density of Cu NPs covered with a thin CaF_2 film has been grown to assess the properties of the CaF_2 film and the Cu NPs. Figure 5a shows the TEM image of a sample composed of a Cu NP film with a nominal thickness of t=1 nm and a CaF_2 layer of t=1 nm, grown on a C-coated Ni grid. Between the particles, a grainy contrast is observed, which corresponds to the polycrystalline nature of the CaF_2 film. This is further confirmed by the high-resolution image (Figure 5b) taken from the red-squared region in Figure 5a, where small crystals, less than 5 nm in size, are clearly visible. These crystals are highlighted by dashed white lines, and the associated Fast Fourier Transform (FFT) shows well-defined spots (indicated by red arrows in the inset), further confirming the crystallinity of the CaF_2.

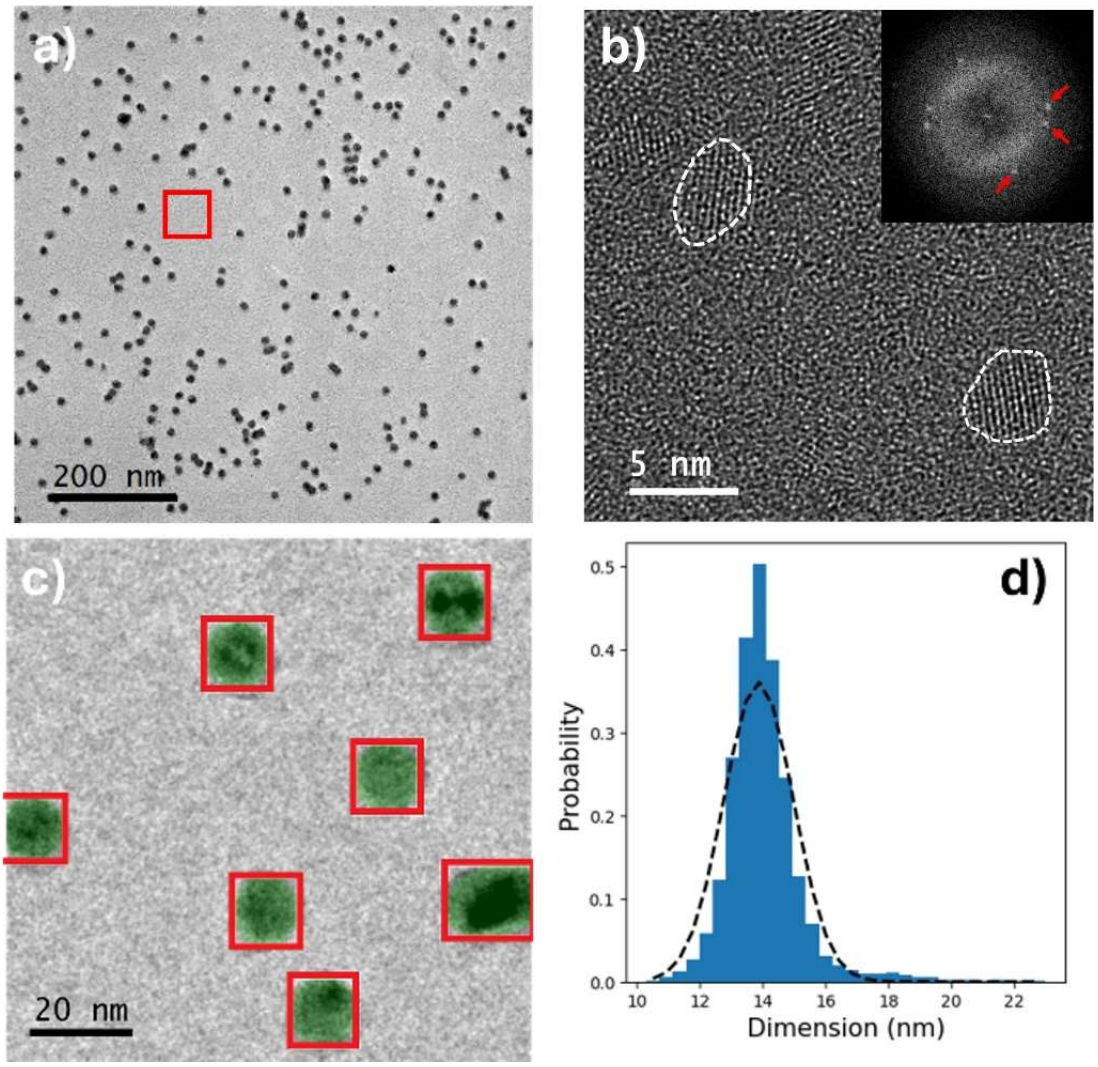

Figure 5. a) TEM image of Cu NPs / CaF_2 sample (1 nm/1 nm). b) HR-TEM acquired in the red-squared region in (a): the small crystals reveal the polycrystalline nature of the CaF_2 film. The inset shows the associated FFT.c) Detection and segmentation of Cu NPs using Mask R-CNN, showing bounding boxes and segmentation masks around individual particles. d) Diameter distribution of Cu NPs obtained from the statistical analysis of 30 TEM images, covering a total of 5392 particles.

The Cu NPs are well-separated and uniformly distributed, although some dimers are present. For a statistical analysis of NP dimensions, TEM images (4096x4096 pixels) were acquired at a low magnification of 74k×, corresponding to a field of view of 830 nm. This magnification is the lowest achievable without deactivating the objective lens, thereby maintaining good image quality. Images like the one presented in Figure 5a are too large to be processed directly with Mask R-CNN, so they were divided into smaller sections of 256×256 pixels, with a stride of 128 pixels to ensure continuity (Figure 5c). For each of these smaller images, Mask R-CNN was able to detect and segment the NPs, identifying bounding boxes around the particles and providing detailed segmentation (green

highlight), as shown in Figure 5c. Finally, Figure 5d presents the diameter distribution of Cu NPs, derived from a statistical analysis performed using Mask R-CNN on 30 TEM images, encompassing a total of 5,392 particles. From this analysis an average diameter <d>=13.8±1.1 nm was obtained. This value is higher than the one obtained by the analysis performed on bare Cu NPs and reported in [14]. Since the working conditions of the NP source were the same in both experiments, it is reasonable to conclude that the highest value of d obtained in this sample is due to the formation of the CaF_2 capping layer evaporated after the Cu NP deposition, as testified also by the crystal fringes in figure 5b. By combining the information on the average diameter obtained by TEM (Figure 5d) and on the average height obtained by AFM (Figure 4 b) it is possible to estimate the average aspect ratio (AR) of the Cu NPs, defined as the ratio between the in-plane and the out-of-plane dimensions. The average AR obtained by dividing the average diameter by the average height of the NPs is $AR=d/h \simeq 1.2\pm0.2$. The AR is a crucial aspect for the plasmonic properties of the NPs [15, 18]. In previous papers, the Cu NPs obtained with similar methods have been found to be in spherical and polyhedral shapes [42-45]. Again, some of the considerations reported previously when SEM measurements were compared to AFM ones still hold, in particular the ones reported in points 1, 3 and possibly 4 (for AFM).

3.2 Electronic and optical properties

3.2.1 XPS characterization

In-situ XPS analysis has been performed on a sample with 12 nm equivalent Cu NPs before and after the deposition of a 6 nm CaF_2 layer. The sample used for the XPS and optical analysis has a significantly higher Cu NP density than the samples used for the morphological characterization, in order to optimize the spectroscopic signal. The Cu 2p and Cu $L_{23}M_{45}M_{45}$ line shapes were measured, to obtain information about the chemical state of Cu atoms in the NP. In particular, the Cu $L_{23}M_{45}M_{45}$ line is highly sensitive to the oxidation state of copper, and it permits to clearly distinguish all the three components [46] Figure 6a and 6b show the Cu 2p and Cu $L_{23}M_{45}M_{45}$ line shapes after the deposition of Cu NPs and after coating with a thick CaF_2 layer (6 nm). The XPS and the AES lines shown in Figure 6 have the same shape before and after CaF_2 deposition, indicating that, copper is in the same chemical state independently on the presence of CaF_2 [44]. Low-intensity satellites are present between the Cu $2p_{1/2}$ and Cu $2p_{3/2}$ in Figure 6a, suggesting the possible presence of a low concentration of Cu (1) and a dominant concentration of metallic Cu [44]. The Cu $L_{23}M_{45}M_{45}$ line shows a dominant peak at 918.6 eV typical of metallic Cu [40]. To have quantitative information on the surface oxidation the Auger spectra have been fitted using the procedure outlined in [39] for Cu, CuO and Cu_2O. A dominant concentration of Cu in the metallic state (~82%) and a low concentration of Cu(1) (~18%) are observed. The mild oxidation of the NPs is probably due to the low residual oxygen pressure in the deposition chamber. The deposition of CaF_2 on top of the NPs does not significantly vary the Cu(1) concentration in the bottom layer of NPs, only causing a slight increase

from 18% to 21%. This result suggests that CaF_2 does not effectively alter the Cu chemical state. The Ca 2p and F1s line-shape (see Supporting Information) are also unaffected.

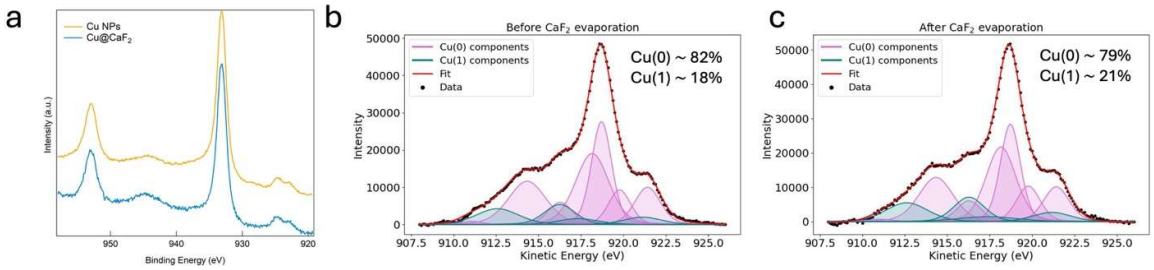

Figure 6. a) Cu 2p XPS spectra obtained from Cu NPs (yellow line) (12 nm) and Cu NPs / CaF_2 sample (12 nm/ 6 nm) (blue line); b) and c) Auger Cu $L_{23}M_{45}M_{45}$ spectra and results of the fitting procedure based on the parameters in ref. [46].

3.2.2 Optical characterization

To understand the effects of the CaF_2 capping on the plasmonic properties and on their stability in atmosphere, the 12 nm/6 nm sample was characterized by UV-Vis absorptance spectroscopy. Figure 7a shows the optical absorptance spectra of the sample composed by 12 nm nominal thickness of Cu NPs coated by 6 nm of CaF_2, acquired immediately after the deposition, with s- and p-polarized radiation. The shape of the two spectra is comparable, suggesting an isotropy of the sample in the surface plane. In the spectra, it is possible to distinguish two different peaks: one in the UV region, peaked at 320 nm, and one in the visible region between 600 and 800 nm. The first peak can be ascribed to the inter-band transition in Cu_2O that is formed during growth (Figure 6). The second absorptance band, peaked at 660 nm, can be ascribed to the LSPR excitation of Cu NPs [15, 16], suggesting that the NPs preserve a metallic core with plasmonic properties. It is known that the LSPR properties and their changes with particle shape and with the surrounding medium (in this case, CaF_2) can be obtained by the classical theory of the optical properties of metallic particles [47]. The plasmonic properties of the proposed structure have been simulated by using the MNPBEM toolbox [24]. The model simulated ellipsoidal metallic Cu NPs , with a diameter equal to the average diameter extracted from Figure 5d (13.8 nm) and height equal to the average one extracted from Figure 4b (11 nm). The impinging radiation is assumed to be linearly polarized in-plane. The NPs are assumed to be immersed in a medium that is a mixture of Cu_2O and CaF_2, lying on fused silica (SiO_2) substrate. Figure 7b shows the simulation performed by accounting for the interaction between two particles, considering one particle with AR=1.25 (average experimental AR) interacting with a particle with the same AR (yellow), with AR = 2 (blue) and with AR=2.5 (red). The binary interactions and the considered change of AR result in a 100 nm shift of the LSPR band towards higher wavelengths with respect to isolated NPs (purple). Figure 7c reports the effect of a very marked change in the composition of the dielectric shell surrounding the metal cores. By changing

the composition from 80% CaF_2 20% Cu_2O (expected to be close to the experimental situation) to 20% CaF_2 80% Cu_2O the absorption peak is shifted by only 30 nm. In the sample investigated the nanoparticles, with a relatively broad distribution of AR, are expected to interact with many close NPs with different ARs, giving rise to a broad absorption peak, compatible with the experimental one shown in Figure 7a. Considering the simulations reported in the Figure 7b and 7c, we expect that the most relevant parameters determining the LSPR position and broadening are related to the interactions between the NPs and the wide distribution of their ARs, while the composition of the surrounding material has a weaker impact.

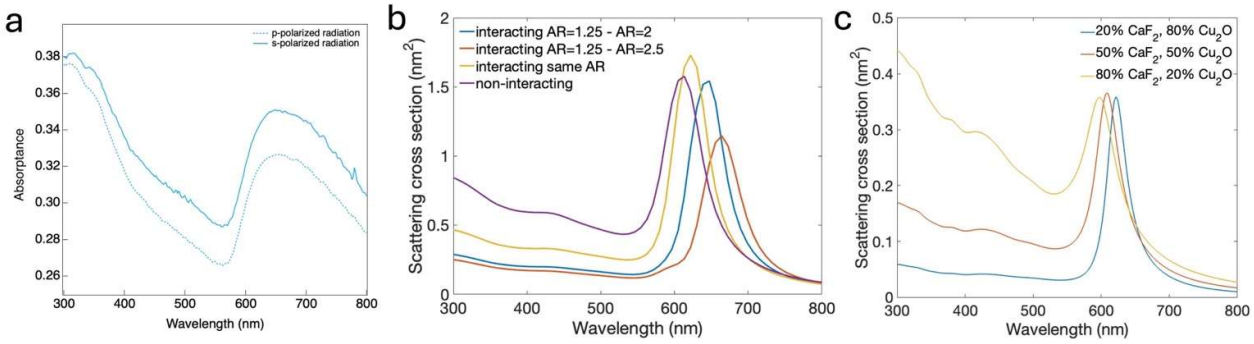

Figure 7. a) UV–Vis absorptance spectra of a Cu NP CaF_2 (12 nm/6 nm) sample using p- and s-polarized radiation (dashed and continuous line respectively); simulated scattering cross section accounting for (b) the interaction between two particles and (c) a very marked change in the composition of the dielectric shell surrounding the metal cores.

3.2.3 Stability

To evaluate the stability of the NPs and the modifications of the plasmonic behavior after exposure to atmosphere, the optical absorptance of the sample described in the previous section was measured 4 months after deposition, during which the film has been left in ambient conditions. Figure 8 shows the optical absorptance spectrum (acquired by p-polarized radiation) directly after the growth (blue line) and after 4 months (blue line). The UV-VIS spectrum taken from a bare Cu NP films after 4 moths of exposure is also reported. While the two spectra from Cu/CaF_2 are very similar, the one from bare Cu NP shows a significant reduction of the LSPR intensity, suggesting that the plasmonic properties of the Cu/CaF_2 film remain almost unmodified even after 4 months in air and indicating an optimal stability in atmospheric conditions, crucial for possible applications of this system.

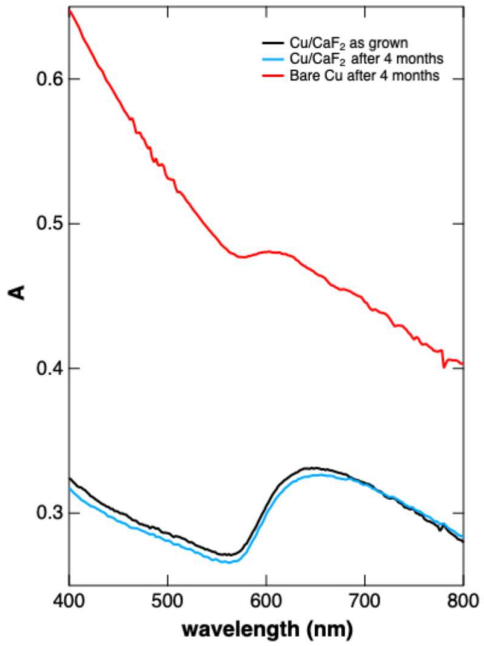

Figure 8. UV–Vis absorptance spectra of a Cu NP film with CaF_2 (12 nm/6 nm) sample as grown (black curve), after 4 months in air (blue curve), and of a bare Cu NP film after 4 months (red curve).

4. Conclusions

Cu NPs have been grown by an inert gas aggregation cluster source and combined with layers of CaF_2 of different thicknesses. The films have been investigated in terms of morphological, electronic and optical properties, to understand the effects of the CaF_2 layer and the stability of the plasmonic resonance. The integration of Mask R-CNN with TEM analysis has enabled precise and automated characterization of nanoparticle dimensions, providing robust statistical insights into particle size distribution across a large dataset. This method opens a new way in TEM data analysis on large NP assemblies, giving more accurate statistics on size distribution, average interparticle distances etc. The deposition of thick CaF_2 layers lead to the NPs being fully buried, resulting in a more complex morphology with extended islands across the sample. The chemical state of the NPs measured in-situ is unaffected by the presence of CaF_2. Although the optical data shows some partial oxidation of the Cu cores, the plasmon of the Cu NPs is preserved, even after a prolonged exposure to air, due to the CaF_2 capping. This result makes the Cu@CaF_2 NP films a promising material for applications in photovoltaics and optoelectronics.

Funding

Project funded under the National Recovery and Resilience Plan (NRRP), Mission 04 Component 2 Investment 1.5 – NextGenerationEU, Call for tender n. 3277 dated 30/12/2021

Award Number: 0001052 dated 23/06/2022

We acknowledge support from the European Union's HORIZON EUROPE framework program for research and innovation (grant agreement n. 101094299 "IMPRESS").

All the authors have approved the final version to be submitted, and they agreed to be accountable for all aspects of the work in ensuring that questions related to the accuracy or integrity of any part of the work are appropriately investigated and resolved.

Data availability statement

Regarding TEM data, the complete dataset is available upon request or through https://zenodo.org/records/15366374

Part of the software used for the TEM data analysis is freely available at the link below Computer Vision Annotation Tool (CVAT) https://zenodo.org/records/12771595, published July 18, 2024 [38]

The remaining data are available upon request.

References

[1] Harry A. Atwater and Albert Polman. Plasmonics for improved photovoltaic devices. Nature Materials, 9(3):205–213, 2010.

[2] S. Pillai and M.A. Green. Plasmonics for photovoltaic applications. Solar Energy Materials and Solar Cells, 94(9):1481–1486, 2010.

[3] Chien-Lun Huang et al., Plasmonic effects of copper nanoparticles in polymer photovoltaic devices for outdoor and indoor applications, Appl. Phys. Lett. 116, 253302 (2020) .

[4] Sumit Malik, Joginder Singh, Rohit Goyat, Yajvinder Saharan, Vivek Chaudhry, Ahmad Umar, Ahmed A. Ibrahim, Sheikh Akbar, Sadia Ameen, and Sotirios Baskoutas. Nanomaterials-based biosensor and their applications: A review. Heliyon, 9(9):e19929, 2023.

[5] Alexandra GellÅLe and Audrey Moores. Plasmonic nanoparticles: Photocatalysts with a bright future. Current Opinion in Green and Sustainable Chemistry, 15:60–66, 2019.

[6] Suljo Linic, Phillip Christopher, and David B. Ingram. Plasmonic-metal nanostructures for efficient conversion of solar to chemical energy. Nature Materials, 10(12):911–921, 2011.

[7] Phillip Christopher, Hongliang Xin, and Suljo Linic. Visible-light-enhanced catalytic oxidation reactions on plasmonic silver nanostructures. Nature Chemistry, 3(6):467–472, 2011.

[8] J. Noguales, J. Sort, V. Langlais, V. Skumryev, S. Suri˜nach, J.S. Muñoz, and M.D. BarÅLo. Exchange bias in nanostructures. Physics Reports, 422(3):65–117, 2005.

[9] Luciano De Sio, Tiziana Placido, Roberto Comparelli, M. Lucia Curri, Marinella Striccoli, Nelson Tabiryan, and Timothy J. Bunning. Next generation thermo-plasmonic technologies and plasmonic nanoparticles in optoelectronics. Progress in Quantum Electronics, 41:23–70, 2015.

[10] Lu-Syuan Jhuang, Gautham Kumar, Fang-Chung Chen, Localized surface plasmon resonance of copper nanoparticles improves the performance of quasi-two-dimensional perovskite light-emitting diodes, Dyes and Pigments, 188, 109204, 2021
[11] Sungi Kim, Jae-Myoung Kim, Jeong-Eun Park, and Jwa-Min Nam. Nonnoble-metal-based plasmonic nanomaterials: Recent advances and future perspectives. Advanced Materials, 30(42), 2018.
[12] Vladimir N. Popok, Sergey M. Novikov, Yurij Yu. Lebedinskij, Andrey M. Markeev, Aleksandr A. Andreev, Igor N. Trunkin, Aleksey V. Arsenin, and Valentyn S. Volkov. Gas-aggregated copper nanoparticles with long-term plasmon resonance stability. Plasmonics, 16(2):333–340, 2020.
[13] Hongbu Yin, Yan Zhao, Xibin Xu, Jie Chen, Xuemin Wang, Jian Yu, Jin Wang, and Weidong Wu. Realization of tunable localized surface plasmon resonance of Cu@Cu_2O core–shell nanoparticles by the pulse laser deposition method. ACS Omega, 4(11):14404–14410, 2019.
[14] Sergio D'Addato, Matteo Lanza, Anthea Boiani, Eleonora Spurio, Samuele Pelatti, Guido Paolicelli, and Paola Luches. Morphology and optical properties of gas-phase-synthesized plasmonic nanoparticles: Cu and Cu/MgO. Materials, 15(13):4429, 2022.
[15] Eleonora Spurio, Samuele Pelatti, Sergio D'Addato, and Paola Luches. Plasmonic properties and stability of au and cu nanoparticles embedded in cerium oxide. Journal of Physics: Condensed Matter, 36(37):375003, 2024.
[16] Eleonora Spurio, Giovanni Bertoni, Sergio D'Addato, Francesca Alimonti and Paola Luches, Mapping the local stoichiometry in Cu nanoparticles during controlled oxidation by STEM-EELS spectral imaging, Nanoscale, 17, 4132-4141, 2025
[17] Sergio D'Addato, Avinash Vikatakavi, Maria Chiara Spadaro, Sergio Valeri, and Luca Pasquali. Physical synthesis and study of Ag@Caf2 core@shell nanoparticles: Morphology and tuning of optical properties. Physica Status solidi (b), 256(7), 2019.
[18] Jacopo Stefano Pelli Cresi, Enrico Silvagni, Giovanni Bertoni, Maria Chiara Spadaro, Stefania Benedetti, Sergio Valeri, Sergio D'Addato, and Paola Luches. Optical and electronic properties of silver nanoparticles embedded in cerium oxide. The Journal of Chemical Physics, 152(11), 2020.
[19] Sergio D'Addato, Daniele Pinotti, Maria Chiara Spadaro, Guido Paolicelli, Vincenzo Grillo, Sergio Valeri, Luca Pasquali, Luca Bergamini and Stefano Corni, Influence of size, shape and core–shell interface on surface plasmon resonance in Ag and Ag@MgO nanoparticle films deposited on Si/SiOx, Beilstein Journal of Nanotechnology 6, 404, 2015.
[20] D.F. Bezuidenhout, Calcium Fluoride (CaF2), page 815–835. Elsevier, 1998.
[21] Mohan V. Jacob, Janina Mazierska, Dimitri Ledenyov, and Jerzy Krupka. Microwave characterization of CaF_2 at cryogenic temperatures using a dielectric resonator technique. Journal of the European Ceramic Society, 23(14):2617–2622, 2003.
[22] Rebecca S Retherford, Robert Sabia, Vincent P Sokira, Effect of surface quality on transmission performance for (111) CaF2, Applied Surface Science, 183, 3–4, 264-269, 2001

[23] Sergio D'Addato, Vincenzo Grillo, Salvatore Altieri, Stefano Frabboni, Francesca Rossi, and Sergio Valeri. Assembly and fine analysis of Ni/MgO core/shell nanoparticles. The Journal of Physical Chemistry C, 115(29):14044–14049, 2011.
[24] Ulrich Hohenester and Andreas Trugler. MNPBEM – a MATLAB toolbox for the simulation of plasmonic nanoparticles. Computer Physics Communications, 183(2):370–381, 2012
[25] Kevin M. McPeak, Sriharsha V. Jayanti, Stephan J. P. Kress, Stefan Meyer, Stelio Iotti, Aurelio Rossinelli, and David J. Norris. Plasmonic films can easily be better: Rules and recipes. ACS Photonics, 2(3):326–333, 2015. PMID: 25950012.
[26] Irving H. Malitson. A redetermination of some optical properties of calcium fluoride. Applied Optics, 2(11):1103, November 1963.
[27] Gorachand Ghosh. Sellmeier coefficients and dispersion of thermo-optic coefficients for some optical glasses. Appl. Opt., 36(7):1540–1546, 1997.
[28] G. Ghosh, M. Endo, and T. Iwasaki. Temperature-dependent Sellmeier coefficients and chromatic dispersions for some optical fiber glasses. Journal of Lightwave Technology, 12(8):1338–1342, 1994.
[29] Kiaming He, Georgia Gkiokari, Piotr Dollàr, Ross Girshik, Mask R-CNN, Proceedings - 30th IEEE Conference on Computer Vision and Pattern Recognition, CVPR 2017, 936-944.
[30] Dangfu Yang, Xian Wang, Haoran Zhangm Zhen-yu Yin, Dong SU, Jun Xu, A Mas R-CNN based particle identification for quantitative shape evolution of granular materials, Powder Technology 392, 296-305, 2021
[31] M. Frei, F. E. Kruis, Image -based size analysis of agglomerated and partially sintered particles via convolutional neural networks, Powder Technology 360, 324-336, 2020.
[32] Max Frei and Frank Einar Kraus, Image-Based Analysis of Dense Particle Mixture via Mask R-CNN, Eng 3(1) 78-98, 2022.
[33] Christoph Mahr, Jakob Stahl, Beeke Gerken, Valentin Baric, Max Frei, Florian F. Krause, Tim Grieb, Marco Schowalter, Thorste Mehrtens, Einar Kruis, Lutz Madler and Andreas Rosenauer, Characterization of mixing in nanoparticle hetero aggregates by convolutional neural networks, Nano Select, 5 (4),2300128 (2024).
[34] LingyuLiao, Zhenfei Sun, Siran Liu, Shining Ma, Kunlong Chen, Tuoe Liu, Yongtian Wang, Weitao Song, Applying a mask R-CNN machine learning algorithm for segmenting electron microscope image of ceramic-bronze casting moulds, Journal of Archaelogical Science 170, 106049, 2024.
[35] Luca Rettenberger, Nathan J. Szymanski, Yan Zeng, Jan Schuetzke, Shilong Wang, Gerbrand Ceder and Markus Reischl, Uncertainty-aware particle segmentation for electron microscopy at varied length scales, npj Computational Materials 10, 124, 2024.
[36] Chistoph Mahr, Jakob Stahl, Beeke Gerken, Florian F. Krause, Marco Schowalter, Tim Grieb, Lutz Madler, Andreas Rosenauer, Ultramicroscopy 265, 114020, 2024.

[37] Hongkun Yu, Chen Chen, Xianzhi Du, Yeqing Li, Abdullah Rashwan, Le Hou, Pengchong Jin, Fan Yang, Frederick Liu, Jaeyoun Kim, Jing Li. TensorFlow Model Garden. https://github.com/tensorflow/models (2020)
[38] Computer Vision Annotation Tool (CVAT) https://zenodo.org/records/12771595, published July 18, 2024.
[39] S. Sajini, B. Pushpa, Design and Evaluation of Image Quality Enhancement to Augment Object Detection and Tracking Framework to Support Visually Impaired Persons, SSRG International Journal of Electronics and Communication Engineering, 10, 9, 52-62, 2023.
[40] M. Getzlaff, J. Bansmann, F. Bulut, R. K. Gebhardt, A. Kleibert, and K. H. Meiwes-Broer, Appl. Phys. A: Mater. Sci. Process. **82**, 95 (2006)
[41] A. Kleibert, F. Bulut, R. K. Gebhardt, W. Rosellen, D. Sudfeld, J. Passig, J. Bansmann, K. H. Meiwes-Broer, and M. Getzlaff, J. Phys.: Condensed Matter **20,** 445005 (2008).
[42] M. Gracia Prinilla, E. Martìnez, G. Silva Pidaurri, E Pérez-Tijerina, Deposition of size-selected Cu nanoparticles by inert-gas condensation, Nanoscale Research Letters **5**, 180 (2010).
[43] O. Kiliàn, J. Kratochvìl, J. Hanus, O. Polonskyi, P. Solar, H. Biederman, Fabrication of Cu nanoclusters and their use for production of Cu/plasma polymer nanocomposite thin films, Thin solid films **550**, 46 (2014).
[44] Mikhail V. Dutka;, Anatoliy A. Turkin, David I. Vainchtein, Jeff Th. M. De Hosson, On the formation of copper nanoparticles in nanocluster aggregation source, J. Vac. Sci. Technol. A **33**, 031509 (2015).
[45] L. Martínez, K. Lauwaet, G. Santoro I. Tanarro, G. J. Ellis, J. Cernicharo, C. Joblin, J. M. Sobrado, R. J. Peláez, V. J. Herrero, Y. Huttel, J. A. Martín-Gago, Precise controlled fabrication, manipulation and *in-situ* analysis of Cu based nanoparticles, Scientific Reports **8,** 7250 (2018).
[46] Mark C. Biesinger. Advanced analysis of copper x-ray photoelectron spectra. Surface and Interface Analysis, 49(13):1325–1334, 2017.
[47] Uwe Kreibig, Michael Vollmer, “Optical properties of metal clusters”, Springer,1993.